Evaluating and improving wave and non-wave stress parametrisations for oceanic flows

Daniel R. Johnston,[a,b]   Callum J. Shakespeare,[b]   and Navid C. Constantinou[c,d]

[a] *School of Science, UNSW Canberra, Australia*
[b] *Research School of Earth Sciences, Australian National University, Australia*
[c] *School of Geography, Earth and Atmospheric Sciences, University of Melbourne, Australia*
[d] *Australian Research Council Centre of Excellence for the Weather of the 21st Century, University of Melbourne, Australia*

ABSTRACT: Whenever oceanic currents flow over rough topography, there is an associated stress that acts to modify the flow. In the deep ocean, this stress is predominantly form drag, caused by the formation of internal waves and other baroclinic motions: processes that act on such small scales most global ocean models cannot resolve. Despite the need to incorporate this stress into ocean models, existing parametrisations are limited in their applicability. For instance, most parametrisations are only suitable for small-scale topography and are either for periodic or steady flows, but rarely a combination thereof. Here we summarise these existing parametrisations and evaluate their accuracy using hundreds of idealised two-dimensional and three-dimensional simulations spanning a wide parameter space. In cases where the parametrisations prove to be in inaccurate, we use our data to suggest improved formulations. Our results thus provide a basis for a comprehensive parameterisation of stress in ocean models where fine scale topography is unresolved.

SIGNIFICANCE STATEMENT: As the ocean flows over topographic features it experiences a force. Such topographic features include abyssal hills that are too small to be accurately described by global ocean and climate models. These forces shape the ocean structure considerably and affect large-scale ocean circulation features, like the Atlantic Meridional Overturning Circulation. Because there is no hope to accurately include these small-scale features in climate projections we need expressions (a.k.a. parametrisations) for the collective force they exert on the ocean. Here, we evaluate existing parametrisations for the force created when an oceanic current flows over an underwater hill by comparing them to the output of small-scale, high-resolution ocean simulations. Compared to previous studies, we cover a much wider range of cases. This allows us to suggest improvements to the existing parametrisations, taking us closer to the goal of developing a general and widely applicable mathematical description of this phenomenon.

1. Introduction

In shallow seas, fast moving currents are subject to significant energy losses from frictional drag along the ocean bottom. However in the deep ocean, where currents are slower, there is still a significant amount of energy dissipation attributed to the formation of internal waves in regions of rough topography (Ledwell et al. 2000; Egbert and Ray 2000, 2001; Naveira Garabato et al. 2013). These waves can cause substantial mixing, which plays a role in nutrient transport and large scale ocean circulation (Sandstrom and

Elliott 1984; Munk and Wunsch 1998; Melet et al. 2013, 2014).

The horizontal extent of many oceanic topographical features is on the scale of $1 - 10$ km. In particular, over half of the ocean floor is covered by abyssal hills and mountains, defined respectively as having a variation in height of $300 - 1000$ m and greater than 1000 m (Harris et al. 2014). Resolving internal waves generated by such features is often not possible with current global ocean models (e.g., Ansong et al. 2015; Kiss et al. 2020), which generally have horizontal resolutions on the order of 10 to 100 km. As a result, it is important to have parametrisations for the effects of internal waves that would be generated at such unresolved hills. Existing parametrisations have mainly focused on computing the energy flux extracted from the flow due to the generation of internal waves (e.g., Llewellyn Smith and Young 2002; Khatiwala 2003; Perfect et al. 2020; Baker and Mashayek 2022). Such a focus is justified, as it has allowed better understanding of the contribution of internal waves to ocean mixing and tidal dissipation. There has however, been far less attention on parametrising the stress due to internal wave formation and other related effects such as blocking (e.g., Winters and Armi 2014) or bottom-trapped tides (e.g., Falahat and Nycander 2015). Such parametrisations are vital to obtaining accurate representations of eddies and tides in global models (Arbic et al. 2019). Notably, the energy loss from a spatially mean flow $\overline{u}$ and topographic stress τ is equal to $\overline{u} \cdot \tau$, and the topographic stress also acts to modify $\overline{u}$. Thus, the topographical stress is a more fundamental quantity to study, in that it can be used to compute energy loss, but this is not necessarily true the other way around.

Due to the complexity of developing a generic parametrisation for stress, existing parametrisations (e.g., Bell 1975;

Corresponding author: Daniel R. Johnston, daniel.johnston@unsw.edu.au

Jayne and St. Laurent 2001; Klymak et al. 2010; Shakespeare et al. 2020) have focused on special cases. For instance, previous studies have treated steady and tidal flows in isolation. However, since the steady and tidal components of a flow can interact (Shakespeare 2020), it is important for existing parametrisations to be extended to mixed flows. Existing parametrisations also have several other assumptions that can reduce their accuracy if incorporated into ocean models. For example, it is often assumed that the topographical height is small (Bell 1975; Shakespeare et al. 2020) or that the latitude is close to 0° (Jayne and St. Laurent 2001; Klymak et al. 2010).

The first goal of this paper is to evaluate the accuracy of existing wave and non-wave stress parametrisations. This is done by comparing theoretical expressions to a large suite of ocean simulations. To limit the scope of these comparisons, we focus on the case of an isolated Gaussian hill in either two or three dimensions. Working with isolated hills is useful as there are only a small number of parameters to consider, allowing us to ensure that the basic physics and scalings of the parametrisations are correct. This is in contrast to other studies (e.g. Jayne and St. Laurent (2001); Buijsman et al. (2015); Shakespeare et al. (2021)) which tend to only test stress parametrisations with global models or more complicated topography. We also note that whilst three-dimensional simulations are physically accurate, they are more computationally expensive than two-dimensional simulations. Moreover, two-dimensional topography may be interpreted as approximating a section of a three-dimensional ridge, which can be sites of significant internal wave generation (Ledwell et al. 2000; Garrett and Kunze 2007). Two-dimensional simulations are thus useful despite being less applicable than three-dimensional models. As a result, our general procedure is to run a large number of tests in two dimensions, and then further analyse any interesting phenomena in three dimensions.

The second goal of this paper is to then suggest improvements to these existing stress parametrisations. This is done using predominantly mathematical or physical arguments that are supported by the simulation data. Notably, one of the common shortcomings in existing parametrisations is the assumption of small topographical height. Large topographical features however, are abundant in the ocean (Harris et al. 2014). Moreover, large isolated hills called seamounts are of interest in ecology, vulcanology and ship navigation (Clark et al. 2010; Watts 2019). Therefore, it is important for existing parametrisations to be extended to such cases. The ultimate goal of this work is the formulation of a more complete parametrisation of wave and non-wave stress for implementation in global ocean models.

The structure of the paper is as follows. In Section 2 we recall some existing drag parametrisations used for tidal, steady and mixed flows. In Section 3 we discuss the setup for our simulations. In Section 4 we then discuss the results

of the simulations, and use these results to evaluate and suggest improvements to each parametrisation. Finally, in Section 5 we discuss the main takeaways from our analysis, and prescribe new parametrisations that depend on the type of flow and scale of topography under consideration.

2. Existing parametrisations

We begin by summarising existing parametrisations for wave and non-wave stress. The parametrisations are categorised depending on the flow in consideration — tidal, steady or mixed. Each parametrisation is expressed in their general form, but we also simplify for the case of an isolated Gaussian hill. For a two-dimensional domain (viewed as cross-section of three dimensional space) with horizontal component $[-L_x/2, L_x/2]$, we define the stress as

$$F_{2d} = \frac{1}{\rho_0} \int_{-L_x/2}^{L_x/2} p_h \frac{dh}{dx} dx, \qquad (1)$$

where $h(x)$ is the bottom topography, $p_h(x)$ the bottom pressure respectively, and ρ_0 is the background density of the sea water. In particular, the stress (1) is the net force per unit length[1] created from the pressure differential across the hill, divided by ρ_0 for convenience. As a result, F_{2d} has units $N\,m^2\,kg^{-1}$ and $\rho_0 F_{2d}$ has units of force per unit length. The sign of F_{2d} is also such that a positive value of F_{2d} corresponds to a force per unit length of magnitude $|\rho_0 F_{2d}|$ acting on the hill in the positive x-direction, along with an equal and opposite force acting on the flow in the negative x-direction. In three dimensions, with a horizontal domain $[-L_x/2, L_x/2] \times [-L_y/2, L_y/2]$, we then define the stress due to a topography $h(x, y)$ as the vector

$$\boldsymbol{F}_{3d} = \frac{1}{\rho_0} \int_{-L_y/2}^{L_y/2} \int_{-L_x/2}^{L_x/2} p_h \boldsymbol{\nabla} h \, dxdy. \qquad (2)$$

Note that $\boldsymbol{F}_{3d}$ has units $N\,m^3\,kg^{-1}$ and $\rho_0 \boldsymbol{F}_{3d}$ has units of force (i.e., N).

In what follows, our domain is as shown in Figure 1, with dimensions $L_x \times L_y \times H$ and a spatially mean zonal flow $U(t)$ over topography $h(x, y)$. For two-dimensional analysis, we restrict ourselves to the $x - z$ plane. Moreover, for the ensuing theoretical analysis in this section, we assume L_x and L_y are large. That is, $L_x, L_y \to \infty$.

Throughout this paper, we use the terms "stress", "form drag" and "internal wave drag" somewhat interchangeably. However, it is to be understood that each of these terms are defined differently. By "stress" we mean the total force (scaled by $1/\rho_0$) acting on the current as per (1) or (2).

---

[1] That is, per unit length in the y-direction. Hence, the two-dimensional stress can be used to compute the total force across a long three-dimensional ridge.
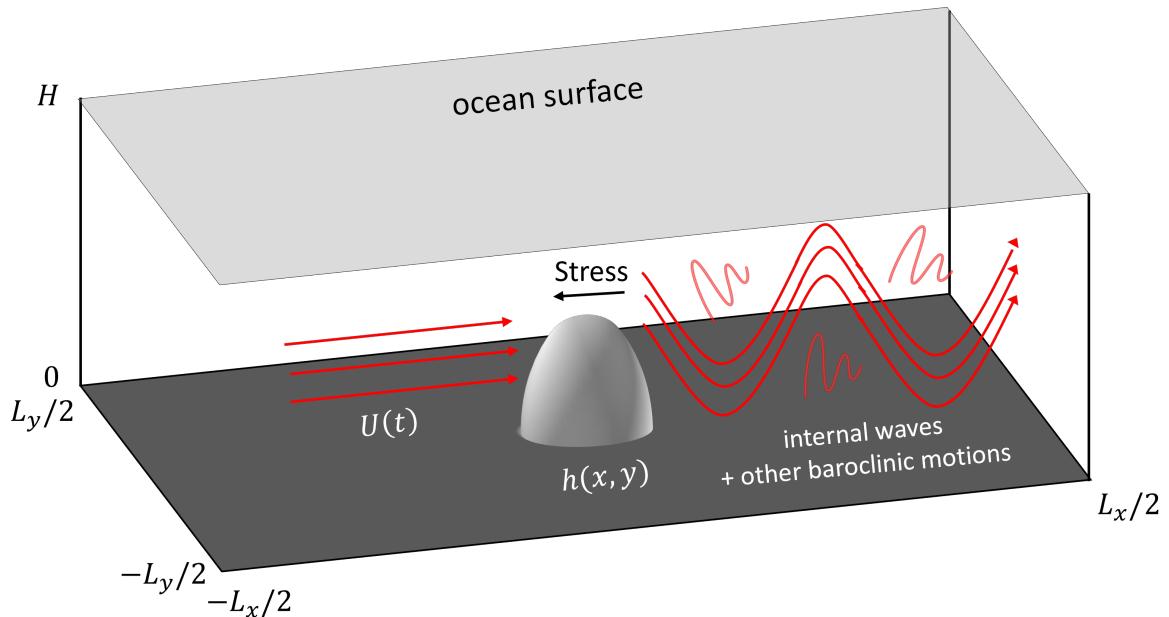
FIG. 1. A schematic of the model domain. A spatially mean flow $U(t)$ interacts with the topography $h(x, y)$ to generate baroclinic motions and an associated stress.

Then, by "form drag" we mean the component of the stress in phase with the current and therefore associated with a mean energy exchange. Finally, "internal wave drag" refers to the component of form drag due to the formation of internal waves. Many existing parametrisations focus only on internal wave drag, which is the dominant component of stress in most idealised scenarios, but not if the flow is "bottom-trapped", sufficiently non-linear or resonant with the topography.

a. Case 1: Tidal Flow

We consider a periodic tidal flow $U(t) = U_{\text{tidal}} \cos(\omega t)$ in the x-direction where U_{tidal} is a constant and ω is the tidal frequency. Tidal flows are a major source of waves and the associated stress impacts the strength of barotropic and internal tides (Ansong et al. 2015; Buijsman et al. 2015). As a result, this flow regime appears to be the main focus of stress in the literature. Here, we restrict our focus to two parametrisations. Namely, an older parametrisation due to Jayne and St. Laurent (2001, hereafter, JSL2001), and a more recent parametrisation due to Shakespeare et al. (2020, hereafter SAH2020).

1) JAYNE AND ST LAURENT PARAMETRISATION

Jayne and St Laurent give a simple estimate for internal wave drag based on a scaling argument derived from the work of Bell (1975). Namely, for each grid cell, they set the stress (in each horizontal dimension) to be proportional to Nh^2u. Here, N is the buoyancy frequency, and h and u are taken to be suitable values of the topography height and tidal velocity in the grid cell. For small $h \ll H$, we can approximate u as $U(t)$ and N as a constant in the vicinity of the topography. Thus, the total stress over a small hill with root mean square height h_{rms} is estimated by

$$F_{\text{JSL}} = \frac{1}{2} \kappa N_B h_{rms}^2 U. \tag{3}$$

Here, κ is the tunable scaling constant in JSL2001 related to the characteristic wavenumber of the topography. Then, N_B denotes the buoyancy frequency at the seabed, and the subscript "JSL" indicates that this is the drag force due to the JSL2001 theory. In line with our units and scaling for stress in (1) and (2), here κ has units of length in three dimensions and is unitless in two dimensions. On the other hand, in JSL2001 the stress is implicitly divided by the horizontal length (in two-dimensions) or area (in three-dimensions) so that κ has units of inverse length. Note that the factor of $1/2$ in (3) could be absorbed into the definition of κ, but we have included it to more closely match the expression given by JSL2001.

Despite the simple form of the JSL2001 parametrisation, this scaling has proven to significantly improve the accuracy of tidal models when compared to observations, and is thus frequently used today (Arbic et al. 2018; Ansong et al. 2015). However, there are some notable limitations of the JSL2001 model. Firstly, the model is only designed for small-scale topography and large ocean depths. Moreover, (3) is latitude-independent, an omission which Jayne

and St Laurent state could be significant when the tidal frequency ω is close to the Coriolis frequency f.

2) Shakespeare, Arbic and Hogg parametrisation

In SAH2020, the authors take a more analytic approach to parametrising tidal flow stress. The main novelty of their work is their treatment of "spring" forces, such as bottom-trapped tides, which do not do any work in the time mean. This is important, because JSL2001 and other early parametrisations compute stress by first considering the time-averaged energy dissipation, and thus do not account for such spring forces. Under standard assumptions, including small topographical height and large ocean depth, SAH2020 give for subcritical latitudes ($|f| < \omega$) and isotropic topography

$$F_{3d} = \frac{\sqrt{(N^2 - \alpha\omega^2)(\omega^2 - f^2)}}{4\pi|\omega|} U \int_0^\infty |\hat{h}(K)|^2 K^2 dK. \quad (4)$$

Here, $\hat{h}$ denotes the Fourier transform of h in t, x and y to transformed variables ω, k and ℓ respectively with $K = \sqrt{k^2 + \ell^2}$. Note that we use the Fourier transform convention

$$\hat{g}(k) \stackrel{\text{def}}{=} \int_{-\infty}^\infty g(x) e^{-ikx} dx. \quad (5)$$

Since we are assuming the topography is isotropic (and independent of time), $\hat{h}$ is a function of the total wavenumber K only, as indicated in (4). We have also introduced a parameter $\alpha \in \{0, 1\}$, whereby

$$\alpha = \begin{cases} 0, & \text{under the hydrostatic assumption,} \\ 1, & \text{otherwise.} \end{cases} \quad (6)$$

In addition, we remark that (4) is only the x-component of the stress, as this is the primary direction of our flow and focus of our analysis.

In SAH2020, a more general expression than (4) is stated which accounts for wave reflections off the surface. However, such reflections are difficult to parametrise, and for an isolated hill the number of waves reflecting back onto the topography is small. Therefore, we omit any reflection terms from (4) for simplicity. Nevertheless, we note that these reflections depend on how the vertical wavelength

$$m = \frac{Nk}{\sqrt{\omega^2 - f^2}}, \quad (7)$$

resonates with the ocean depth H. As a result, we expect (4) to have small deviations from the actual stress as the geometry of the topography, and the variables N, ω and f are varied.

In the case of an isolated Gaussian with half-width W, whereby

$$h(x, y) = h_0 e^{-(x^2 + y^2)/(2W^2)} \quad (8)$$

we obtain from (4)

$$F_{3d} = \frac{\pi\sqrt{\pi}}{4} W \frac{\sqrt{(N^2 - \alpha\omega^2)(\omega^2 - f^2)}}{\omega} h_0^2 U. \quad (9)$$

Note that in the limit $N \gg \omega$ (or $\alpha = 0$) and $\omega \gg |f|$, (9) is of the same form as (3). The expression for supercritical (bottom-trapped) latitudes $|f| \geq \omega$ is similar, but with the stress out of phase with velocity. In particular, for a Gaussian hill

$$F_{\text{SAH3d}} = \frac{\pi\sqrt{\pi}}{4} W \omega^{-1} h_0^2 U_{\text{tidal}} \times$$
$$\times \begin{cases} \sqrt{(N^2 - \alpha\omega^2)(\omega^2 - f^2)} \cos(\omega t), & |f| < \omega, \\ \sqrt{(N^2 - \alpha\omega^2)(f^2 - \omega^2)} \sin(\omega t), & |f| \geq \omega, \end{cases} \quad (10)$$

where the subscript SAH3d indicates that this is the three-dimensional stress due to the SAH2020 theory. In a subsequent paper (Shakespeare et al. 2021), the authors also give a parametrisation for two dimensions. Namely, for a Gaussian hill $h(x) = h_0 e^{-x^2/(2W^2)}$,

$$F_{\text{SAH2d}} = \omega^{-1} h_0^2 U_{\text{tidal}} \times$$
$$\times \begin{cases} \sqrt{(N^2 - \alpha\omega^2)(\omega^2 - f^2)} \cos(\omega t), & |f| < \omega, \\ \sqrt{(N^2 - \alpha\omega^2)(f^2 - \omega^2)} \sin(\omega t), & |f| \geq \omega. \end{cases} \quad (11)$$

Note that (11) is identical to (10) except without the factor of $\pi\sqrt{\pi}W/4$. To obtain (10) and (11) one also needs to assume that N is constant. In the more physical setting where N is varying function of depth, Shakespeare et al. (2021) suggest taking N to be the value of the buoyancy frequency at the mean ocean depth.

b. Case 2: Steady Flow

We now consider a constant steady flow U in the x-direction. Under such a flow, the internal waves formed are called lee waves. These lee waves have zero Eulerian frequency (i.e. are steady at a fixed point), and are formed with intrinsic frequency depending on the topography and the magnitude of U. This leads to some added complexities compared to the tidal case, where the internal waves have the same intrinsic frequency as the tide. In particular, for steady flows there is a greater dependency on the Froude number

$$Fr \stackrel{\text{def}}{=} \frac{Nh}{U}. \quad (12)$$

For large Froude numbers, the system becomes highly non-linear and harder to parametrise. Namely, when $Fr \gtrsim 1$, this non-linearity manifests as blocking or splitting, which

can significantly decrease the formation of lee waves (Nikurashin et al. 2014).

As in the tidal case, we also focus on two parametrisations for steady flows, treating the cases of small and large Froude numbers separately. The first, which is based on the linear theory of Bell (1975), is an idealised theory assuming lee waves form without the effects of a high Froude number. The second, is a semi-empirical parametrisation due to Klymak et al. (2010, hereafter, KLP2010). The KLP2010 parametrisation focuses instead on a regime where most of the flow is blocked, and unable to surmount the topography to form lee waves. These two parametrisations therefore look at different aspects of the wave and non-wave stress, and so both are useful in obtaining a wholistic parametrisation.

1) Bell parametrisation for steady flows

In the work of Bell (1975), an expression for the time-mean stress due to lee waves is provided. In three dimensions, their expression for the (x-component of) stress is

$$F_{\text{Bell3d}} =$$
$$= \frac{1}{4\pi^2} \iint \frac{k\,|\hat{h}(k,\ell)|^2}{\sqrt{k^2+\ell^2}} \sqrt{[N^2 - \alpha(kU)^2][(kU)^2 - f^2]}\,\mathrm{d}k\mathrm{d}\ell \tag{13}$$

where α is as in (6) and the integrals are taken over all real values of k and ℓ under the restriction $|f| \leq |kU| < \infty$ for hydrostatic ($\alpha = 0$) and $|f| \leq |kU| \leq N$ for non-hydrostatic ($\alpha = 1$). As we are taking the flow speed to be constant, the lee wave stress is non-zero in the time-mean and there is not an equivalent bottom-trapped spring force as in the SAH2020 tidal parametrisation theory. However, it is worth noting that (13) can readily be obtained by repeating the arguments in SAH2020 for a steady flow. The two-dimensional equivalent of (13) is then

$$F_{\text{Bell2d}} =$$
$$= \frac{1}{2\pi} \int\limits_{\substack{|f| \leq |kU| \\ \alpha|kU| \leq N}} |\hat{h}(k)|^2 \sqrt{[N^2 - \alpha(kU)^2][(kU)^2 - f^2]}\,\mathrm{d}k. \tag{14}$$

We now consider the case of an isolated Gaussian hill of height h_0. In general, (13) and (14) do not simplify much further unless one wishes to express the parametrisations in terms of incomplete Bessel functions. However, in the special case at the equator ($f = 0$) with a hydrostatic

assumption ($\alpha = 0$), we have

$$F_{\text{Bell3d}}(\alpha = f = 0) = \frac{\pi\sqrt{\pi}}{4} W N h_0^2 U, \tag{15}$$

$$F_{\text{Bell2d}}(\alpha = f = 0) = N h_0^2 U, \tag{16}$$

which is the same as what one obtains in the tidal case (cf. (10) and (11)).

Bell's parametrisations are derived in the case $Fr \ll 1$. For higher Froude numbers the lee wave flux saturates as non-linear blocking and splitting effects take hold (Nikurashin et al. 2014). In more recent energy flux parametrisations (e.g., Baker and Mashayek 2022), a simple scaling is used to account for this phenomena. Namely, let E denote the internal wave energy flux and E_{Bell} denote the energy flux predicted by the Bell (1975) theory. Then for some critical Froude number Fr_c one sets

$$E = \left(\frac{Fr_c}{Fr}\right)^2 E_{\text{Bell}}. \tag{17}$$

whenever $Fr \geq Fr_c$. The standard values of Fr_c used are 0.7 in two dimensions, and 0.4 in three dimensions (Nikurashin et al. 2014).

2) Klymak, Legg and Pinkel parametrisation

In KLP2010, a form drag parametrisation is obtained for when the Froude number Fr is very large, whereby blocking effects are the dominant form of stress. Their parametrisation is derived using numerical simulations for two-dimensional Gaussian hills under the hydrostatic assumption and $f = 0$. The full expression for the form drag in KLP2010 is

$$F_{\text{KLP}} = N h_0^2 U_m \left[1 + \pi \frac{U_m}{N h_0} - 2\pi^2 \left(\frac{U_m}{N h_0}\right)^2 \right] \tag{18}$$

where h_0 is the hill height and

$$U_m = \frac{H}{H - h_0} U. \tag{19}$$

In KLP2010, a factor of $\pi/2$ actually appears out the front of (18). However, this is the result of a small algebraic error so that the factor is actually $\pi/3 \approx 1$.

For $Fr \gg 1$, the second and third terms in (18) are small, so that this parametrisation is nearly equivalent to the linear lee wave stress given in (16). The main difference is the scaling of U by $H/(H-h)$, which represents the increase in velocity as the flow moves over the narrower channel above the hill. This suggests that when $f = 0$, an approximate $N h_0^2 U$ scaling could be accurate for both low and high Froude numbers.

To limit the scope of this paper we focus on the cases $Fr \ll 1$ (Bell (1975) theory) and $Fr \gg 1$ (KLP2010 theory) discussed above. However, there are also intermediate regimes $Fr \approx 1$ that one can consider. In this regard, "hybrid" parametrisations have been developed in both the atmospheric (Garner 2005; Lott and Miller 1997) and oceanic (Klymak et al. 2021; Perfect et al. 2020) literature. This style of parametrisation has been successfully compared with both global models (Trossman et al. 2013, 2016) and observations (Trossman. et al. 2015). Such parametrisations generally represent the stress as the sum of a propragating (wave) component near the crest of the topography, and a non-propagating (blocked) component at the base of the topography.

c. Case 3: Mixed Flow

Finally, we consider a mixed flow in the x-direction of the form

$$U(t) = U_{\text{mean}} + U_{\text{tidal}} \cos(\omega t), \quad (20)$$

where U_{mean} and U_{tidal} are constants. Compared to the tidal and steady cases, very little work has been done on mixed flows. We thus hope that our subsequent simulations can shine a light on previously unconsidered regimes.

A priori, we expect that the stress for a mixed flow should have a mean (F_m) and periodic (F_p) component i.e.

$$F_{3d} = F_m + F_p \cos(\omega t + \phi) \quad (21)$$

where ϕ denotes a phase shift. A naive parametrisation would be to assume that the mean (steady) and tidal components of the flow do not interact. That is, F_m is independent of U_{tidal} and F_p is independent of U_{mean}, so that F_m and F_p can be directly computed from the parametrisations in the steady and tidal cases respectively. In terms of a more sophisticated parametrisation, we now discuss a more general version of the Bell (1975) theory.

Although we previously discussed the Bell (1975) theory for steady flows, Bell also gives a more general expression for mixed flows. Namely, in three dimensions, Bell gives the following formula for the x-component of the time-mean stress (cf. (13))

$$F_{m,3d} =$$
$$= \frac{1}{4\pi^2} \sum_{n=-\infty}^{\infty} \iint \frac{k\,|\hat{h}(k,\ell)|^2}{\sqrt{k^2+\ell^2}} \sqrt{(N^2 - \alpha\omega_n^2)(\omega_n^2 - f^2)} \times$$
$$\times J_n^2 \left(\frac{kU_{\text{tidal}}}{\omega} \right) dk\, d\ell, \quad (22)$$

where $\omega_n = n\omega + kU_{\text{mean}}$, J_n is the nth-order Bessel function of the first kind, and the integrals are taken over all real values of k and ℓ under the restriction $|f| \leq |\omega_n| < \infty$

if $\alpha = 0$ and $|f| \leq |\omega_n| \leq N$ if $\alpha = 1$. The two-dimensional equivalent, which we denote $F_{m,2d}$ is then given by

$$F_{m,2d} =$$
$$= \frac{1}{2\pi} \sum_{n=-\infty}^{\infty} \int_{\substack{|f| \leq |\omega_n| \\ \alpha|\omega_n| \leq N}} |\hat{h}(k)|^2 \sqrt{(N^2 - \alpha\omega_n^2)(\omega_n^2 - f^2)} \times$$
$$\times J_n^2 \left(\frac{kU_{\text{tidal}}}{\omega} \right) dk. \quad (23)$$

There are some notable features of (22). Firstly, if $U_{\text{tidal}} = 0$ then (22) reduces to the same expression in the steady flow case (14). Moreover, if $U_{\text{mean}} = 0$, we have $F_{m,3d} = F_{m,2d} = 0$. We also note that $J_0(0) = 1$ and $J_n(0) = 0$ for $n > 0$ but in general $|J_0(x)| \leq 1$ and $|J_n(x)| \geq 0$. This can be interpreted as the lee wave energy ($n = 0$) being transferred to higher modes ($n > 0$) in the presence of a tidal flow (Shakespeare 2020). However, since $|J_n(x)| \ll |J_0(x)|$ for $n \geq 1$ and small x, the time-mean stress predicted by (22) and (23) is often not too different from the case of a purely steady flow.

Finally we note that the Bell parametrisation (22) only gives a small glimpse of understanding on how to parametrise stress for mixed flows. Like the Bell parametrisation for a steady flow, (22) only applies in the linear regime, where the topographical height is assumed to be small. Bell's parametrisation also does not tell us anything about the periodic component of stress F_p. Thus, we will primarily analyse our simulation data for F_p by simply comparing it with the tidal case where $U_{\text{mean}} = 0$. However, one should expect some impact of the mean flow on the periodic stress given that the mean flow will act to Doppler shift the tidal frequency ω.

3. Numerical Model

We use *Oceananigans* (Ramadhan et al. 2020; Wagner et al. 2025) to model flow over an isolated Gaussian hill in two or three dimensions. Importantly, the GPU capability of Oceananigans allows us to run several hundred simulations whilst using only a modest amount of computational resources (see also Silvestri et al. (2024)). In what follows, we focus on the setup in three dimensions, as the two-dimensional simulations are essentially the same but with only one grid cell in the y-direction and improvements in the resolution. For more precise details of the setup see Johnston (2025), which contains the base code used for each simulation.

By default, our domain was set to be $L_x = L_y = 500$ km long and wide, $H = 1.5$ km deep and centred on a symmetric Gaussian hill $h(x,y) = h_0 e^{-(x^2+y^2)/(2W^2)}$ with height h_0 and half-width $W = 5$ km. Our domain was periodic in the horizontal x-y directions, and bounded in the vertical. To capture the features near the hill, the domain grid was

stretched to give a horizontal spacing of $\Delta x = \Delta y \approx 700$ m around the hill, smoothly varied to $\Delta x = \Delta y \approx 2100$ m at the edge of the domain. Similarly, the vertical grid spacing was set to be $\Delta z \approx 7.5$ m in the bottom half of the domain, smoothly varied to $\Delta z \approx 22.5$ m near the surface.

To keep the hill isolated, we artificially damped wave features at the horizontal boundaries by introducing a "sponge layer" in the horizontal regions $[-L_x/2, -L_x/4]$, $[L_x/4, L_x/2]$, $[-L_y/2, -L_y/4]$ and $[L_y/4, L_y/2]$. In particular, the horizontal diffusivity and horizontal viscosity coefficients were smoothly varied from 0 near the hill, to 2000 m^{2}s^{-1} in the outer regions of the domain. Note that everywhere the above-mentioned coefficients were the same. Similarly, the buoyancy and horizontal velocity were relaxed to their initial conditions at the horizontal boundaries to prevent wave features from propagating across the periodic boundary and obfuscating the results.

For each simulation, we specified constant values for background stratification (N), hill height (h_0), hill width (W), ocean depth (H), Coriolis frequency (f), and tidal frequency (ω) if required. Depending on the whether we were concerned with a tidal, mean or mixed case, we also specified the flow speeds U_{mean} and U_{tidal} (see (20)). The velocity is initialised as $\boldsymbol{u}(t = 0) = (U_{\text{mean}} + U_{\text{tidal}}, 0, 0)$ and the buoyancy is initialised with $b(t = 0) = N^2 z$. The velocity is then forced analogously to the simulations by Shakespeare et al. (2021) or Klymak (2018) to maintain a background zonal velocity $U(t) = U_{\text{mean}} + U_{\text{tidal}} \cos(\omega t)$. In particular, a forcing of $F_y = f U_{\text{mean}}$ is added to the y-momentum equations and a forcing of

$$F_x = \frac{f^2 - \omega^2}{\omega} U_{\text{tidal}} \sin(\omega t) \qquad (24)$$

is added to the x-momentum equations. Our general procedure was to run a test using reference values for N, h_0, W, H, f, ω, U_{mean} and U_{tidal}, before varying each parameter individually to determine their impact on the stress. For the purely tidal or steady flow tests, these default parameters are listed in Table 1. Note that the bottom-trapped tests are run at $90°S$ which, although unphysical, is fine in a simulation and allows us to study a regime whereby bottom-trapped effects truly dominate. For the mixed flow case, the parameters will either be the same as the tidal case with a mean velocity of $U_{\text{mean}} = 0.1$ m s^{-1} added, or the same as the mean case with a tidal velocity of $0.1 \cos(\omega t)$ m s^{-1} added. This will be made clear in the text. Also note that the default values of h_0 and H vary slightly between the two and three-dimensional tests. This is due to it being more difficult to achieve sufficient resolution for small hills in the three-dimensional case.

The x-component of the stress was directly computed as in (2):

$$F_{3d} = \frac{1}{\rho_0} \int\limits_{-L_y/2}^{L_y/2} \int\limits_{-L_x/2}^{L_x/2} p_h \frac{\partial h}{\partial x} dx dy, \qquad (25)$$

where $p_h(x, y)$ is the pressure corresponding to the grid cell directly above the hill at horizontal position (x, y).

For efficiency, all simulations were run in hydrostatic mode. The unimportance of non-hydrostatic processes for the stress is reflected by the parametrisations in Section 2, whereby the hydrostatic ($\alpha = 0$) and non-hydrostatic ($\alpha = 1$) parametrisations are essentially the same provided the buoyancy frequency N is large compared to the wave frequency. Each three-dimensional tidal test was run for 200 hours, whereas each three-dimensional steady test was run for 100 hours. We found that 100 hours was generally long enough to reach a near-equilibrium state, with the slightly longer test time given for tidal tests as to have more full tidal cycles to perform a statistical analysis on. Since two-dimensional tests were much less computationally expensive, we decided to run them for even longer (750 hours) to improve accuracy and detect any notable effects that only appeared at later times. All simulations used time-step of 7.5 minutes, and an output interval of 15 minutes.

4. Results and Evaluation

We now compare the parametrisations in Section 2 with the numerical data from the model described in Section 3. We consider results separately depending on the type of flow (tidal, steady or mixed) and the number of dimensions (two or three).

For each of the purely tidal flow simulations, we assume that (the x-component of) the stress is periodic and of the form

$$\text{Stress}(t) = A \cos(\Omega t + \phi) \qquad (26)$$

for some determinable values of the amplitude A, frequency Ω and phase ϕ. To compute these values, we fit the last 200 simulation outputs (or 40 hours) to a sine curve using the Python package *pyestimate* (Humblet 2024). To calculate uncertainty, we then recompute these values for the last 100 outputs and the last 101–200 outputs, recording the difference from the initially obtained values.

For each of the purely steady flow simulations, we use the average value of the stress over the last 20 hours of simulation. The uncertainty is then computed using the minimum and maximum values of the stress during these last 20 hours.

Finally, for the mixed flow simulations, we assume the stress was of the form (cf. (21))

$$\text{Stress}(t) = F_m + F_p \cos(\Omega t + \phi), \qquad (27)$$

TABLE 1. The default parameter values used for the tests with a purely tidal or steady flow in either two dimensions (2d) or three dimensions (3d). For the tidal flow tests, the choice of ω and f (and thus latitude) will be made clear in the text. The parameters for the steady flow tests vary depending on whether we are interested in a low or high Froude number $Fr = Nh_0/U_{\text{mean}}$ regime.

	Tidal	Steady ($Fr \lesssim 1$)	Steady ($Fr \gg 1$)
N (s^{-1})	0.004	0.002	0.005
h_0 (m)	100	20 (2d) or 30 (3d)	500
W (m)	5000	5000	5000
H (m)	1500	1500 (2d) or 1250 (3d)	1500
f (s^{-1})	$-5 \cdot 10^{-5}$ or $-1.46 \cdot 10^{-4}$	$-2.53 \cdot 10^{-5}$	0
Latitude ($^\circ S$)	20 or 90	10	0
ω (s^{-1})	$1.4 \cdot 10^{-4}$ or $7.3 \cdot 10^{-5}$	–	–
U_{mean} (m s^{-1})	0	0.2	0.1
$Fr = Nh_0/U_{\text{mean}}$	–	0.2 (2d) or 0.3 (3d)	25
U_{tidal} (m s^{-1})	0.1	0	0

with both a mean component F_m and a periodic component $F_p \cos(\Omega t + \phi)$. To compute F_m and F_p we again use the *pyestimate* package to fit the last 200 simulation outputs to a shifted sine curve of the form (27). The uncertainty in F_m and F_p is obtained by recomputing these values using the last 100 outputs and 101–200 outputs and recording any difference.

a. Tidal flow in two dimensions

We first consider tidal flow over an isolated hill in two dimensions. For each simulation, the computed stress is compared to the parametrisations in Section 2a. Figure 2 shows this comparison for the parametrisation F_{SAH2d} (11) when the parameters U_{tidal}, N, f, W, H and h_0 are varied. For most of these simulations, the flow is forced with the semi-diurnal M_2 constituent, with $\omega = 1.4 \times 10^{-4}$ s^{-1}. The only exception is the bottom-trapped ($|f| > \omega$) tests, whereby we use the diurnal K_1 constituent ($\omega = 7.3 \times 10^{-5}$ s^{-1}). This is because bottom-trapped effects are more common for diurnal constituents than semi-diurnal constituents (since the frequency ω is smaller).

In general, the parametrisation F_{SAH2d} performs well compared to the simulations. However, in most cases the theoretical prediction slightly underestimates the stress. This is to be expected as the parametrisations from JSL2001 and SAH2020 are derived in an idealised regime whereby the topographical height and flow speed are assumed to be small. There are thus other non-linear effects that are not accounted for which could contribute to the drag. For instance, calculations of Balmforth et al. (2002) show that the energy flux should increase by around 14%

above the linear theory for isolated Gaussians as the steepness parameter

$$s = \frac{Nkh_0}{\sqrt{\omega^2 - f^2}} \tag{28}$$

goes from 0 to 1, which we expect should also translate to form drag. Note that with the default parameters used here, $s \approx 0.6$ for the dominant wavenumber.

Looking at Figures 2a and 2b, we see that the predicted linear scaling by U_{tidal} and N matches the simulations almost precisely. The same is true for the $\sqrt{\omega^2 - f^2}/\omega$ scaling for f (Figure 2c), highlighting the importance of accounting for latitude in tidal stress, which was neglected in the JSL2001 parametrisation.

However, for the simulations varying W, H and h_0 (Figures 2d–2h), there are some larger discrepancies between the computed stress and F_{SAH2d}. Firstly for the tests varying W we see a small increase in the drag as W increases. Note that a priori we do expect some dependence of the stress on W despite it not appearing in F_{SAH2d}. This is because a wider hill gives more area for waves reflected off the surface to interact with topography. However, it is not clear whether this should always correspond to an increase in stress as observed in the simulations.

Next, for the tests varying H and h_0 we find that, provided $|f| < \omega$, the flow in the vicinity of the hill speeds up as it moves over the narrow channel at the top of the hill. Thus, to better model the stress for the H and h_0 tests we use the velocity scaling

$$U_m(t) = \frac{H}{H - h_0} U(t), \tag{29}$$

inspired by the steady flow parametrisation F_{KLP} (see (19)). Here, the factor of $H/(H - h_0)$ is the ratio of the ocean depth H away from the hill, to the ocean depth $H - h_0$ at the centre of the hill. For medium-sized hills replacing $U(t)$ with $U_m(t)$ in F_{SAH2d} more accurately matches our simulation data. However, we also find that the scaling $U_m(t)$ "saturates" around $h_0 \approx H/2$ in the sense that using the velocity scaling

$$\widetilde{U}_m(t) = \begin{cases} \frac{H}{H-h_0}U(t), & h_0 \leq H/2 \\ 2\,U(t), & h_0 > H/2 \end{cases} \tag{30}$$

yields better results for large values of h_0. This is shown in Figures 2e–2g, whereby incorporating $\widetilde{U}_m(t)$ into the F_{SAH2d} parametrisation gives a stress profile that closely matches the simulation data. The only exception is when the hill crest is close to the surface ($h_0 \approx H$) and the stress plateaus (Figure 2g).

For bottom-trapped ($|f| \geq \omega$) flows we found that the F_{SAH2d} parametrisation remains relatively accurate as h_0 increases (Figure 2h). This is expected as such flows have a different velocity profile compared to the $|f| < \omega$ case. Namely, when $|f| \geq \omega$, the flow still speeds up at the top of the hill but is slowed down or "trapped" at the base of the hill. Thus in this case, it is not accurate to use the $\widetilde{U}_m$ scaling, which assumes the current speeds up along the entire length of the hill.

Finally, we analyse the frequency and phase of the simulated stress and how it compared to the parametrisations. For the tests varying f, this is shown in Figure 3. Here, the F_{SAH2d} parametrisation suggests that the frequency of the stress should be equal to ω. Then, in the absence of wave reflections, the stress should be in phase with $U(t)$ when $|f| < \omega$ and then 90° (or 1/4 of a tidal period) out of phase with $U(t)$ when $|f| > \omega$. Note that we give the phase in hours, obtained by multiplying ϕ (from (26)) by $\omega/2\pi$. Most of our simulations accurately reflect the predicted values from F_{SAH2d}, usually giving a stress profile with the predicted frequency (Figure 3a) and within half an hour of the predicted phase (Figure 3b). This provides further support for using the SAH2020 parametrisation over the JSL2001 parametrisation, which does not account for the phase shift when $|f| > \omega$.

b. Tidal flow in three dimensions

Our results for tidal flow in three dimensions are analysed analogously to our results in two dimensions. Note that in what follows, we compute the x-component of the stress amplitude, frequency and phase. Figure 4 shows a comparison between F_{SAH3d} and the simulation data when the parameters U_{tidal}, W, f and h_0 were varied. Plots of the stress frequency and phase are also included for tests that vary the latitude (or equivalently f).

Similar to the two-dimensional case, the simulations varying U_{tidal}, W and f (Figures 4a–4c) qualitatively reflect the scaling predicted by the F_{SAH3d} parametrisation. However, for tests varying f there is a notably larger quantitative deviation between the simulated stress and that predicted by F_{SAH3d}. This is particularly true near the critical latitude where $|f| = \omega = 1.4 \cdot 10^{-4} \text{ s}^{-1}$. To account for this, we note that the F_{SAH3d} parametrisation is derived assuming a small excursion parameter $\epsilon = k\bar{u}/\omega$. As a result of this assumption, the temporal and spatial terms of the governing equations cancel when $|f| = \omega$. Therefore, the fact that the simulated stress is non-zero at the critical latitude represents the limitation of such an assumption, and our results indicate that this effect may be more impactful in three dimensions.

We now consider tests varying h_0. In the bottom-trapped ($|f| > \omega$) case, the simulated data matches the scaling predicted by the F_{SAH3d} parametrisation (Figure 4d). However, for our choice of parameters, the simulated stress underestimates F_{SAH3d} more than in the two-dimensional case. In particular, F_{SAH3d} overestimated the simulation data by an average of 146% in three dimensions, compared to 118% in two-dimensions. In the case where $|f| < \omega$ there is then a qualitative difference between the computed stress profile and that predicted by F_{SAH3d}, depending on whether the hill width W is small or large (Figures 4f and 4g). To account for this difference, we let $\widetilde{F}_{SAH3d}$ be equal to F_{SAH3d} but with the velocity scaling $\widetilde{U}_m$ (Equation (30)) discussed in the two-dimensional setting. For large W (Figure 4f), the scaling of the simulated stress is the same as in the two-dimensional case. Namely, it matches the stress profile predicted by $\widetilde{F}_{SAH3d}$ until $h_0 \approx H$. However, for our default width $W = 5000$ m, the simulated stress only matches $\widetilde{F}_{SAH3d}$ for small–medium values of h_0 (Figure 4e). Then, for $h_0 \gtrsim 500$ m, the stress is much closer to the unscaled F_{SAH3d} parametrisation. This is not entirely unexpected as provided W is not too large, we expect some of the current to flow around the hill, rather than be forced over the top as in the two-dimensional case.

Finally, we remark that, as with the two-dimensional case, the frequency and phase accurately matches the values predicted by the SAH2020 theory (Figures 4g and 4h). However, the most notable difference in three dimensions is a smoother transition from the stress being in phase when $|f| < \omega$ to being 90° out of phase when $|f| > \omega$. Nevertheless, this effect was only clear when $|f|$ was very close to ω so that the phase predicted in F_{SAH3d} is still accurate for almost all values of f.

c. Steady flow in two dimensions

For two-dimensional tests with a steady flow we compare the computed stress with the parametrisations F_{Bell2d} and F_{KLP} from Section 2. In particular, tests with low Froude
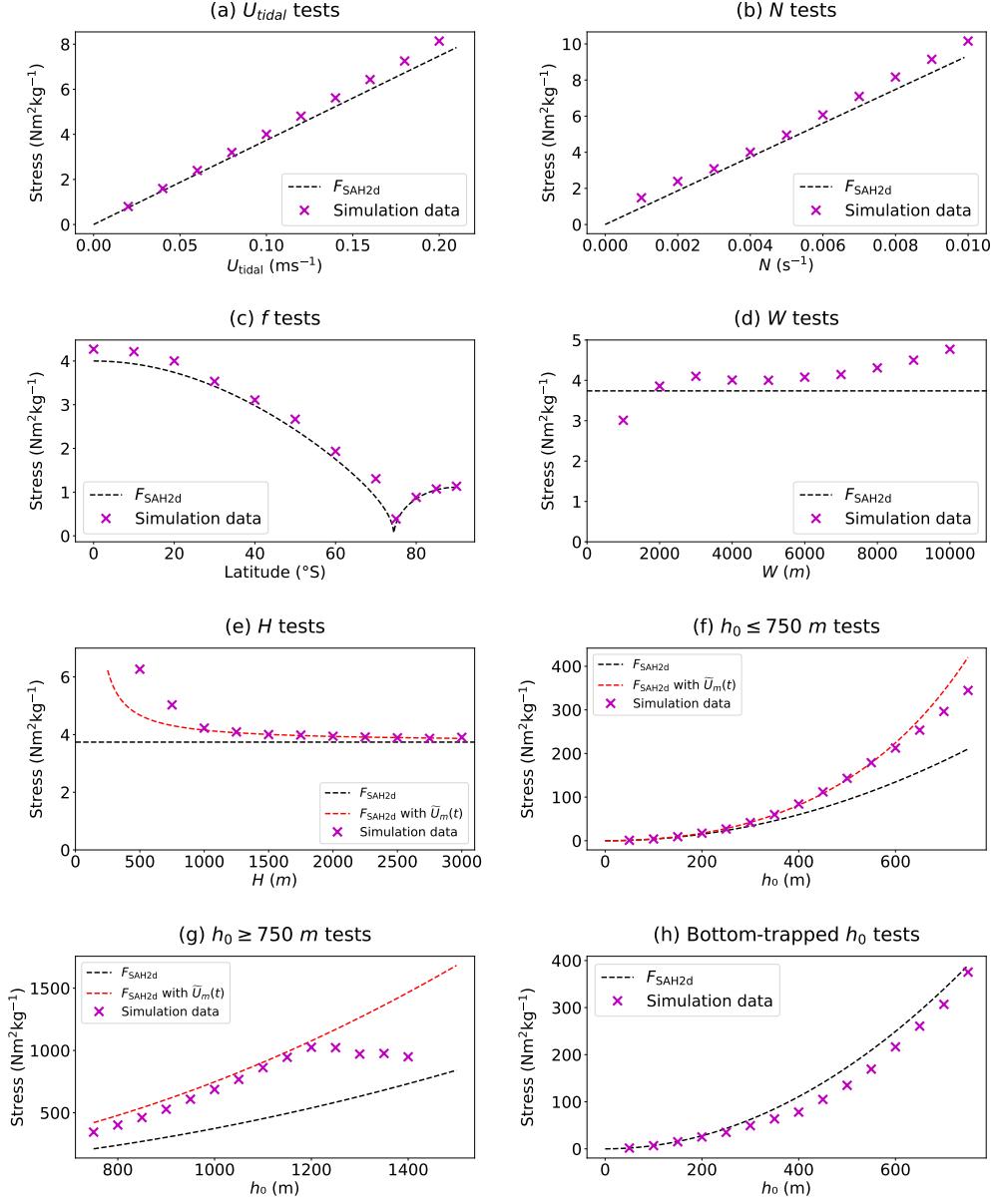
FIG. 2. The amplitude of the oscillatory stress given by F_{SAH2d} and the simulation data for two-dimensional tidal flow. The default parameters for each test are as in Table 1 with $\omega = 10^{-4}$ s^{-1} (M_2 tide) at a latitude of $20°S$ ($f = 5 \cdot 10^{-5}$ s^{-1}). The only exception was the bottom-trapped tests (Figure (h)) which used $\omega = 7.3 \cdot 10^{-5}$ s^{-1} (K_1 tide) at a latitude of $90°S$ ($f = 1.46 \cdot 10^{-4}$ s^{-1}). In all tests, the uncertainty in the computed stress was less than 3% so the (small) error bars have been omitted.

numbers $Fr \lesssim 1$ are compared with F_{Bell2d} and tests with high Froude numbers $Fr \gg 1$ are compared with F_{KLP}.

Figure 5a shows our comparison between the simulated data and F_{Bell2d} for Froude numbers in the range $0.1 - 1$. We see that although the scaling used in Bell's theory is generally accurate, F_{Bell2d} typically underestimates the stress by about 50%, and even more so as the Froude number approaches 1. Hence, Bell's parametrisation should ideally be adjusted to depend on Fr. In this regard, one

could define a scaled parametrisation

$$\widetilde{F}_{\text{Bell2d}} = \frac{1}{A_1 - B_1 (Nh_0/U)} F_{\text{Bell2d}}, \qquad (31)$$

for constants A_1, B_1, and $Fr \lesssim 1$. Note that the linear trend line in Figure 5a corresponds to the values $A_1 = 0.71$ and $B_1 = 0.46$. However, a parametrisation of the form (31) still does not describe the full behaviour of the stress in the regime $Fr \lesssim 1$. Namely, in Figure 5b we also see a non-
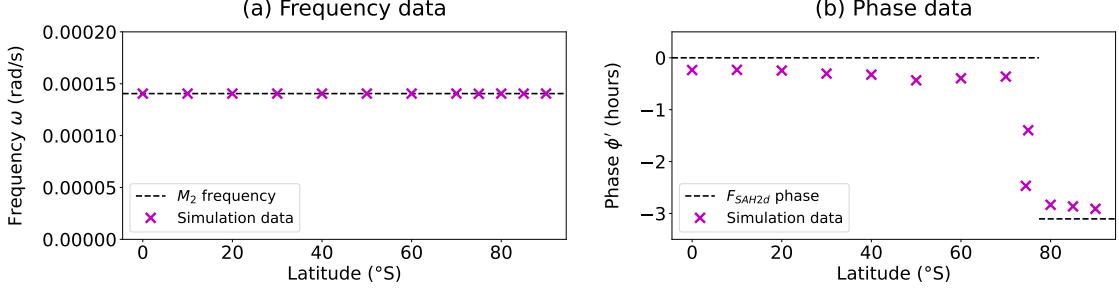
FIG. 3. The fitted frequency and phase of the stress for our two-dimensional tidal flow simulations varying latitude. Here, the phase $\phi' = \phi \times (\omega/2\pi)$ is given in hours as opposed to radians (cf. (26)). In each test, the uncertainty was less than 10^{-6} rad/s in the frequency, and less than 0.05 hours in the phase so the (small) error bars have been omitted.

linear relationship between the stress and latitude. This reinforces that, even for low Froude numbers, non-wave and non-linear effects manifest that are not accounted for by Bell's theory. We also remark that the trend line in Figure 5a is the opposite to what one gets with energy flux calculations. That is, as the Froude number increases, one reaches a saturation of lee waves and Bell's parametrisation (for energy flux) becomes an overestimate (see (17)).

Figures 5c–5e then show our comparison between the simulated data and F_{KLP} for large Froude numbers and $f = 0$. Here, the approximately linear scaling of N and U in F_{KLP} seems to be very accurate (Figures 5c and 5d). On the other hand, the height scaling of $h_0^2 H/(H-h_0)$ overestimates the stress as h_0 gets large (Figure 5e). Our results indicate that a simpler scaling than that in F_{KLP} is more accurate. In particular, if we set

$$F_{\text{2d}} = C_1 N h_0^2 U \tag{32}$$

for some suitable constant C, then we get much closer to the drag from the simulations. For $C_1 = 1.4$ this is shown in Figure 5e. Moreover, using (32) as opposed to F_{KLP} gives a valid result for lower Froude numbers when F_{KLP} is negative (and thus unphysical).

We also ran a few tests with rotation added to the high Froude number simulations. In this case, the stress was unstable and increased by several fold. Upon analysing the simulation data, we found that for these cases significant mixing occurred downslope, and gradually reduced the downstream stratification to zero. This phenomena is reminiscent of atmospheric downslope windstorms, which can occur near large-scale topography on land (see (e.g., Peltier and Clark 1979; Scinocca and McFarlane 2000). However, this dramatic effect was only observed in our two-dimensional tests, since in three-dimensions the presence of a lateral flow helps to stabilise the stratification. Therefore, such effects are mostly unphysical and we have not attempted to parametrise them here.

d. Steady flow in three dimensions

For steady flow tests in three-dimensions, we again compare simulations with low Froude numbers $Fr \lesssim 1$ to the Bell (1975) theory. However, for tests with high Froude numbers $Fr \gg 1$, it does not make sense to compare our results directly to the KLP2010 theory as this theory was only derived in the two-dimensional case. Thus, for high Froude numbers, we instead focus on how the stress scales with different parameters.

Figure 6 shows a comparison between the stress from our simulations and F_{Bell3d} when the parameters h_0, N, U, f and W are varied. For tests varying h_0 and N (Figure 6a) we find, similar to the two-dimensional case, that F_{Bell3d} underestimates the stress but still gives a mostly accurate scaling (i.e. $F_{\text{3d}} \propto N h_0^2$). However, for tests that vary U, f and W (Figure 6b), we see that F_{Bell3d} significantly underestimates the stress as the Rossby number

$$Ro \stackrel{\text{def}}{=} \frac{U}{|f|W} \tag{33}$$

decreases. In this regard, it is worth noting that via a change of variables, F_{Bell3d} can be expressed as

$$F_{\text{Bell3d}}\left(\alpha = 0,\ h(x,y) = h_0 e^{-(x^2+y^2)/2W^2}\right) =$$

$$= \text{Re}\left(\int_0^{2\pi}\int_0^{\infty} \tilde{K} e^{-\tilde{K}^2} \cos^2\theta \sqrt{\tilde{K}^2 - \frac{1}{Ro^2 \cos^2\theta}}\, d\tilde{K} d\theta\right) N h_0^2 W \rho_0 \tag{34}$$

where $\tilde{K} = W\sqrt{k^2 + \ell^2}$ and $(kW, \ell W) = (\tilde{K}\cos\theta, \tilde{K}\sin\theta)$. From (34) we see that as Ro increases so too does the lee wave stress. Therefore, a possible explanation for the discrepancy between F_{Bell3d} and the simulation data is that as Ro decreases, fewer lee waves are formed and the stress is instead generated by other non-linear motions such as partial blocking (see e.g., Trossman et al. 2016; Klymak et al. 2021). To parametrise this phenomenon, we note that from Figure 6b the ratio F_{Bell3d}/F_{3d} has a clear linear
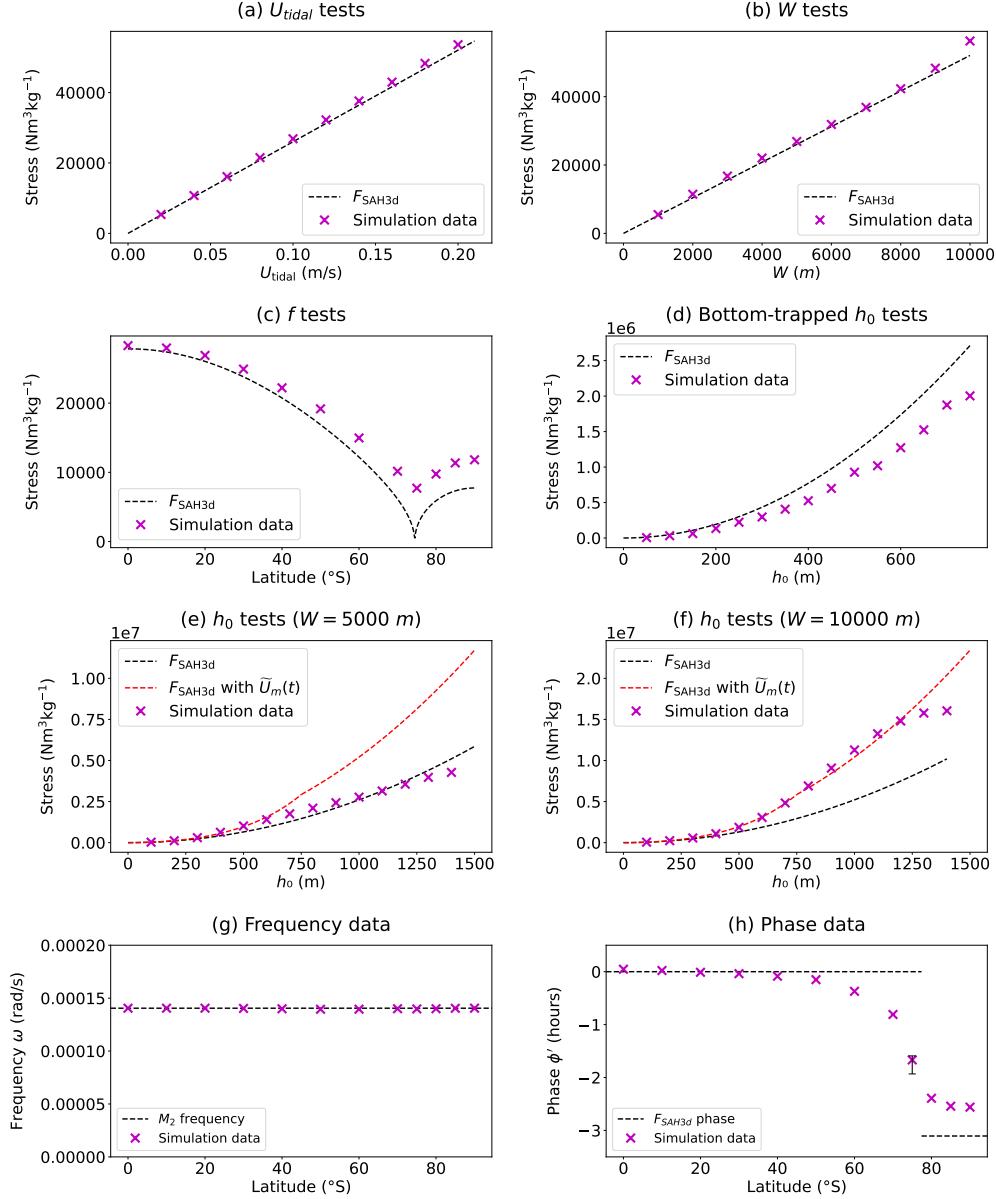
FIG. 4. The amplitude of the oscillatory stress given by F_{SAH3d} and the simulation data for three-dimensional tidal flow (panels (a)–(f)), and the frequency and phase of the stress as the latitude is varied (panels (g) and (h)). The default values for each test were the same as the two-dimensional case (see Figure 2 and Table 1). In panels (a)–(g), the uncertainty in the computed values was less than 10% so the (small) error bars have been omitted. In Figure (h), error bars have only been included in the single case where the uncertainty in the phase was greater than 0.1 hours.

dependence on the ratio fW/U. In particular, our data points give a correlation coefficient between $F_{\mathrm{Bell3d}}/F_{3d}$ and fW/U of $R^2 = 0.89$. This suggests that we should use the scaling

$$\widetilde{F}_{\mathrm{Bell3d}} = \frac{1}{A_2 - B_2|fW/U|} F_{\mathrm{Bell3d}} \qquad (35)$$

for some constants A_2 and B_2 and $Fr \lesssim 1$. The linear trend line in 6b corresponds to $A_2 = 1.34$ and $B_2 = 0.88$.

Certainly, (35) should only be applied for small values of $|fW/U|$ so that the denominator $A_2 - B_2|fW/U|$ remains positive.

Figure 7 shows the results of our tests for the high Froude number $Fr \gg 1$ regime. In this case, we find that the stress deviates significantly from the approximate Nh_0^2WU scaling found in other regimes. Instead we find that the stress obeys a quadratic law $F_{3d} \propto h_0WU^2$, similar to what one expects in the atmosphere (e.g., Lott and Miller 1997). In
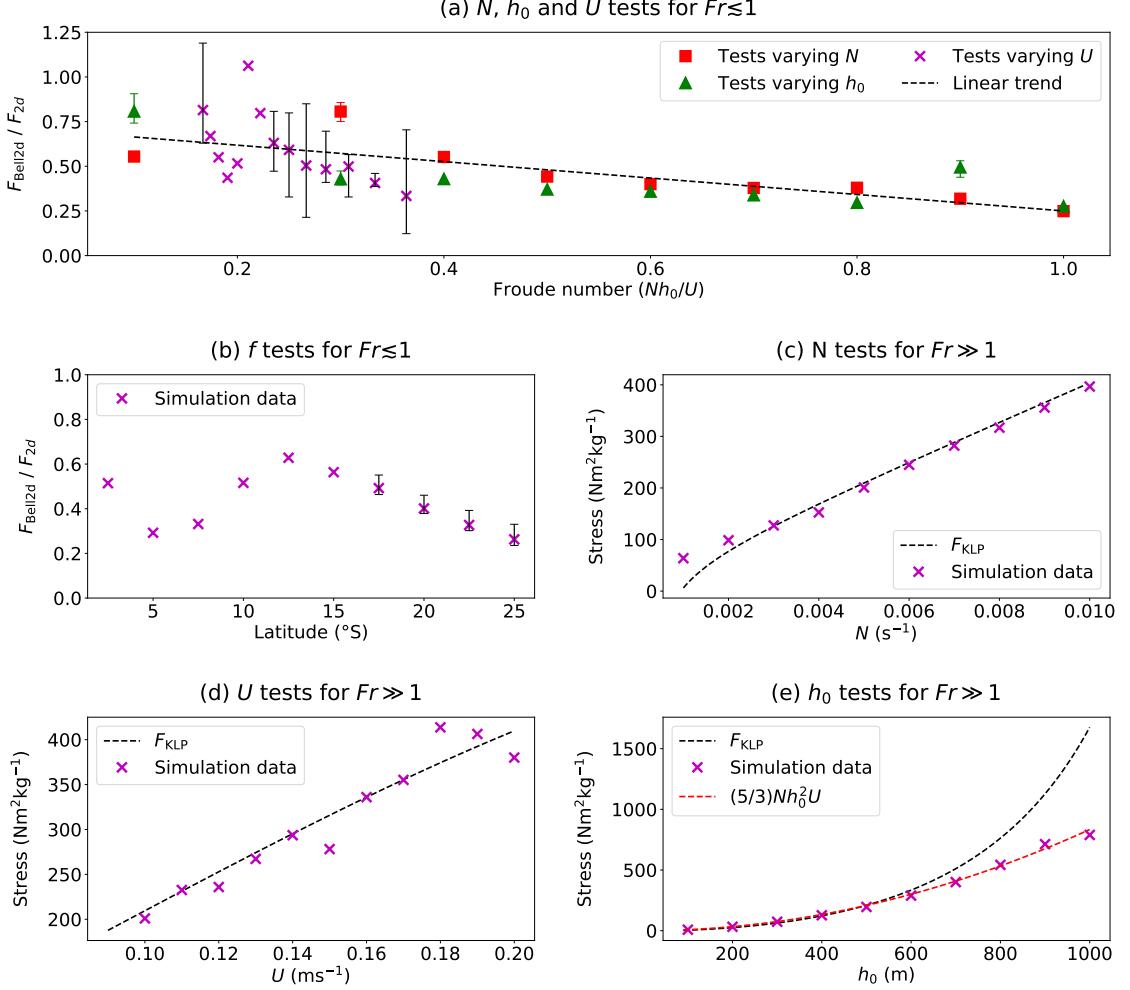
FIG. 5. A comparison of the stress predicted by the Bell (1975) and KLP2010 parametrisations with our simulation data for two-dimensional steady flow. The default parameters are as in Table 1 and error bars are shown whenever the uncertainty in the stress was greater than 10%.

fact, the simple parametrisation $F_{3d} = h_0 W U^2$ works remarkably well for our choice of parameters. The stress then appears to be mostly independent of N and f (Figures 7d and 7e); only increasing or decreasing by small amounts as these parameters are varied. We note however, that for larger values of f, our computed value of the stress has a large uncertainty. These results can be directly compared to recent work of Klymak et al. (2021) which involved a similar analysis but with many, randomly distributed obstacles. Klymak et al. also observed this f independence for the stress but an approximately linear dependence on N for high Froude numbers. Therefore, we do not expect the stress to remain independent of N for more complicated non-isolated topography.

e. Mixed flow in two dimensions

We now analyse our results for mixed flows with a horizontal velocity of the form (20) and stress of the form (27). In what follows we let $\widetilde{F}_m$ and $\widetilde{F}_p$ be the values for F_m and F_p if U_{tidal} or U_{mean} are set to be zero respectively. This lets us discern the impact of a tidal flow on a steady flow and vice versa. Note that values for $\widetilde{F}_m$ and $\widetilde{F}_p$ are obtained using simulations as in the purely steady or tidal flow cases. In Figure 8 we show our computed values of $F_m/\widetilde{F}_m$ and $F_p/\widetilde{F}_p$ for a range of parameters. When the Froude number is small ($Fr \lesssim 1$) these ratios are also compared to the expected ratio from Bell's parametrisations defined in Sections 2b and 2c (Figures 8e and 8f).

To compute the uncertainty in our values of $F_m/\widetilde{F}_m$ and $F_p/\widetilde{F}_p$, we define $F_m^-, \widetilde{F}_m^-, F_p^-, \widetilde{F}_p^-$ and $F_m^+, \widetilde{F}_m^+, F_p^+, \widetilde{F}_p^+$ to respectively be the lower and upper values of uncertainty for each quantity. The lower and upper uncertainties in
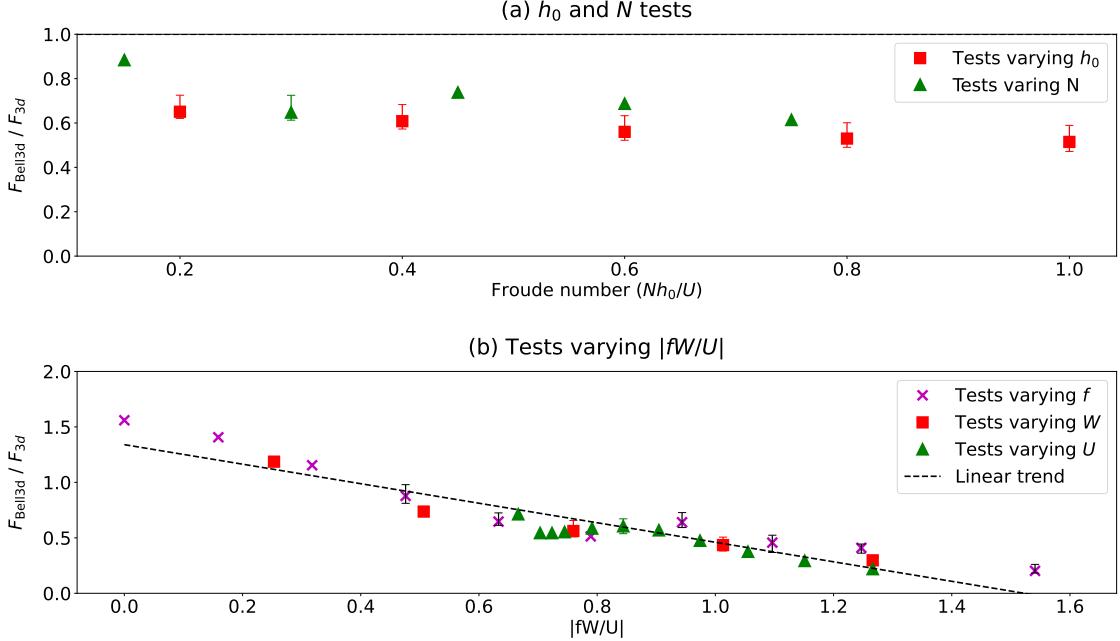
FIG. 6. A comparison of the stress predicted by the Bell (1975) parametrisation (F_{Bell3d}) and the simulation drag (F_{3d}) for three-dimensional steady flows with low Froude number ($Fr \lesssim 1$). The default parameters are as in Table 1 and error bars are shown whenever the uncertainty in the computed stress is greater than 10%.

$F_m/\widetilde{F}_m$ and $F_p/\widetilde{F}_p$ are then given by

$$\left(\frac{F_m}{\widetilde{F}_m}\right)^{\pm} = \frac{F_m^{\pm}}{\widetilde{F}_m^{\mp}} \qquad \text{and} \qquad \left(\frac{F_p}{\widetilde{F}_p}\right)^{\pm} = \frac{F_p^{\pm}}{\widetilde{F}_p^{\mp}}. \qquad (36)$$

First we consider our results for the mean component of the stress F_m. In general, for both low and high Froude numbers, we find that $F_m/\widetilde{F}_m \approx 1$, suggesting that the naive parametrisation $F_m = \widetilde{F}_m$ is accurate for a wide range of parameters. However, in some regimes we find that F_m notably exceeds $\widetilde{F}_m$. This is most evident in Figure 8e, where F_m can be over two times larger than $\widetilde{F}_m$ for small values of U_{mean}. This is reflected by Bell's formula (23), whereby as $U_{\text{mean}} \to 0$ we have $\omega_0 \to 0$ so that the $n = 0$ term becomes small and the $n \geq 1$ terms associated with the tide become more dominant. However, we note that using Bell's parametrisation, F_m exceeds $\widetilde{F}_m$ by more than what is reflected by the simulation data.

Our simulations also indicate that Bell's parametrisation is very inaccurate for larger Froude numbers $Fr \geq 1$, so that this parametrisation should not be extended to such a case. For instance, for our h_0 tests in Figure 8c we have $2 \leq Fr \leq 26$ and $F_m/\widetilde{F}_m \approx 1$. However, Bell's parametrisation gives the substantially larger value $F_m/\widetilde{F}_m = 21.38$.

Next we consider our results for the periodic component of the stress F_p. Similar to the mean component, we find in most regimes that $F_p/\widetilde{F}_p \approx 1$, thereby further highlighting the accuracy of the naive parametrisation $F_p = \widetilde{F}_p$.

The most notable exception is near critical latitudes when $|f| \approx \omega$ (Figure 8b). This is to be expected as the steady component of the flow acts to Doppler shift the tidal frequency ω. Therefore when $|f| = \omega$, we expect F_p to not approach zero unlike $\widetilde{F}_p$ (see (11)), leading to a large value of the ratio $F_p/\widetilde{F}_p$.

For low Froude numbers (Figures 8e and 8f) we also observe a dependence of $F_p/\widetilde{F}_p$ on the parameters U_{mean} and W. In particular, $F_p/\widetilde{F}_p$ notably exceeds 1 for large values of U_{mean} (Figure 8e), and small values of W (Figure 8f). This is likely linked to the fact that the classical lee wave frequency kU_{mean} depends explicitly on U_{mean} and implicitly on W. In particular, with the Fourier convention in (5), the wavenumber spectrum for a Gaussian hill $h(x) = h_0 e^{-x^2/(2W^2)}$ is

$$\hat{h}(k) = h_0 W \sqrt{2\pi} e^{-k^2 W^2/2}. \qquad (37)$$

It appears difficult however, to convert these observations into an accurate analytic parametrisation for F_p.

We also investigate the change in phase from a purely tidal flow to a mixed flow. In what follows we set ϕ_{tidal} and ϕ_{mixed} to be the respective phases for a purely tidal and a mixed flow with the same choice of parameters (besides the presence of a mean flow $U_{\text{mean}} = 0.1 \text{ m s}^{-1}$ in the mixed case). When $|f| \ll \omega$, we find that both ϕ_{tidal} and ϕ_{mixed} are approximately in phase with the velocity $U(t)$. However, as f increases, ϕ_{tidal} increasingly deviates from ϕ_{mixed}.
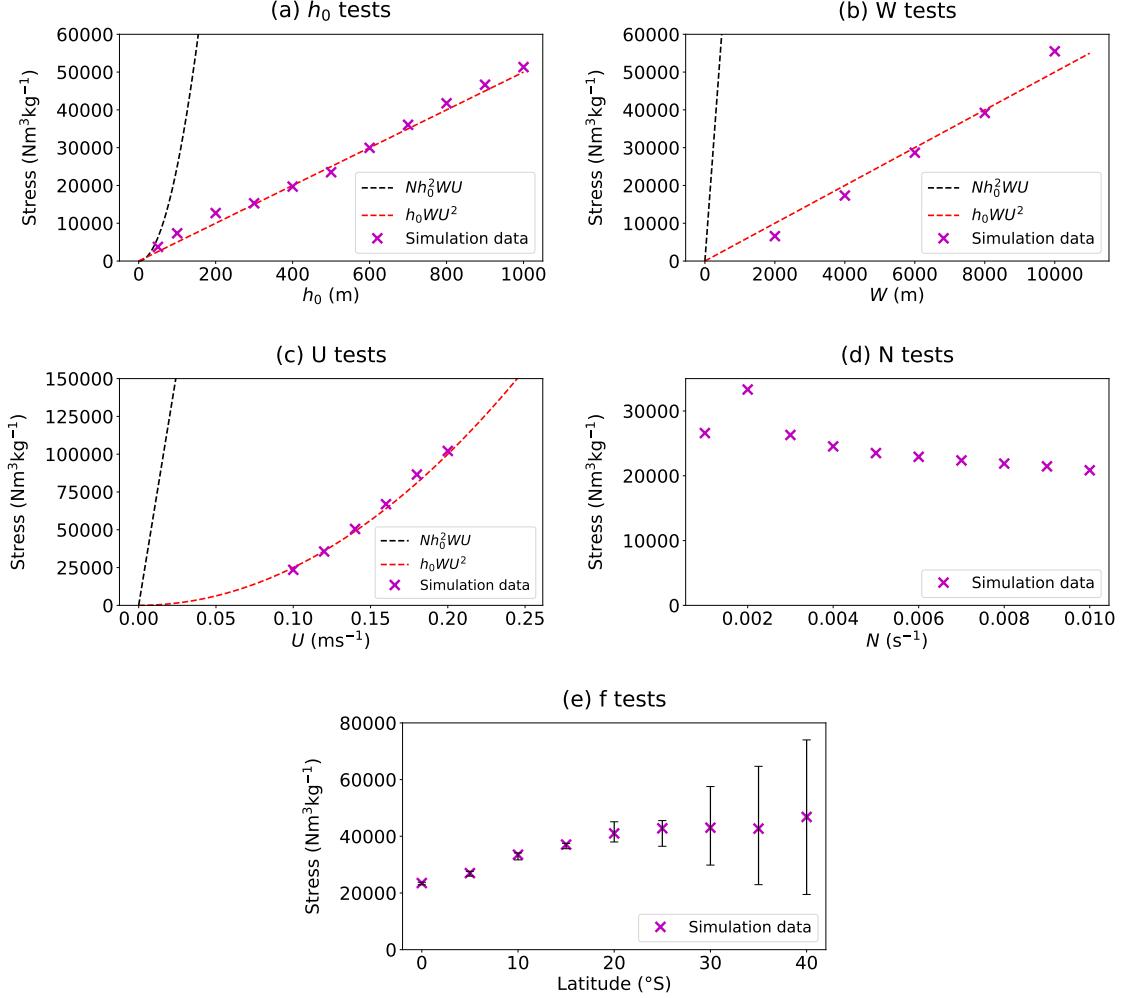
FIG. 7. Topographic stress for three-dimensional steady flows with high Froude number ($Fr \gg 1$). In panels (a)–(c), the drag from the simulation data is compared with both a linear $Nh_0^2 WU$ and quadratic $h_0 WU^2$ scaling. The default parameters are as in Table 1. Note that in panels (a)–(d) the uncertainty in the computed stress was always less than 10% so the (small) error bars have been omitted.

In Figure 8g this is shown for our tests varying latitude (cf. Figure 8b), whereby the difference between ϕ_{tidal} and ϕ_{mixed} reaches about 5 hours at $80°S$. This effect was also observed in a small number of supplementary simulations (not shown) for other tidal constituents besides M_2.

f. Mixed flow in three dimensions

Finally we consider mixed flows in three dimensions, with our results for this regime shown in Figure 9. Note that we use the same notation as in Section 3e).

Like the two-dimensional case, we also find that $F_m/\widetilde{F}_m \approx 1$ and $F_p/\widetilde{F}_p \approx 1$ for the majority of tests. In fact, this approximation holds true even more often than the two-dimensional case (cf. Figure 8). Of particular note is the far less dramatic increase in $F_p/\widetilde{F}_p$ near the critical latitude $|f| \approx \omega$. There is however, a distinct increase in

the ratio $F_m/\widetilde{F}_m$ as h_0 increases, which was not observed in the two-dimensional setting.

The other key difference in the three-dimensional setting is the value of the phase for mixed flows. In Figure 9g we see that the mixed flow phase is close to 0 so that the total stress is given by

$$F_{3d} = F_m + F_p \cos(\omega t + \phi) \tag{38}$$

with $\phi \approx 0$. By comparison, in two dimensions we found that ϕ was much larger as $|f|$ increased (Figure 8g). Such an effect is also in contrast to the purely tidal flow case, whereby the phase ϕ approaches $-\pi/2$ for large $|f|$.
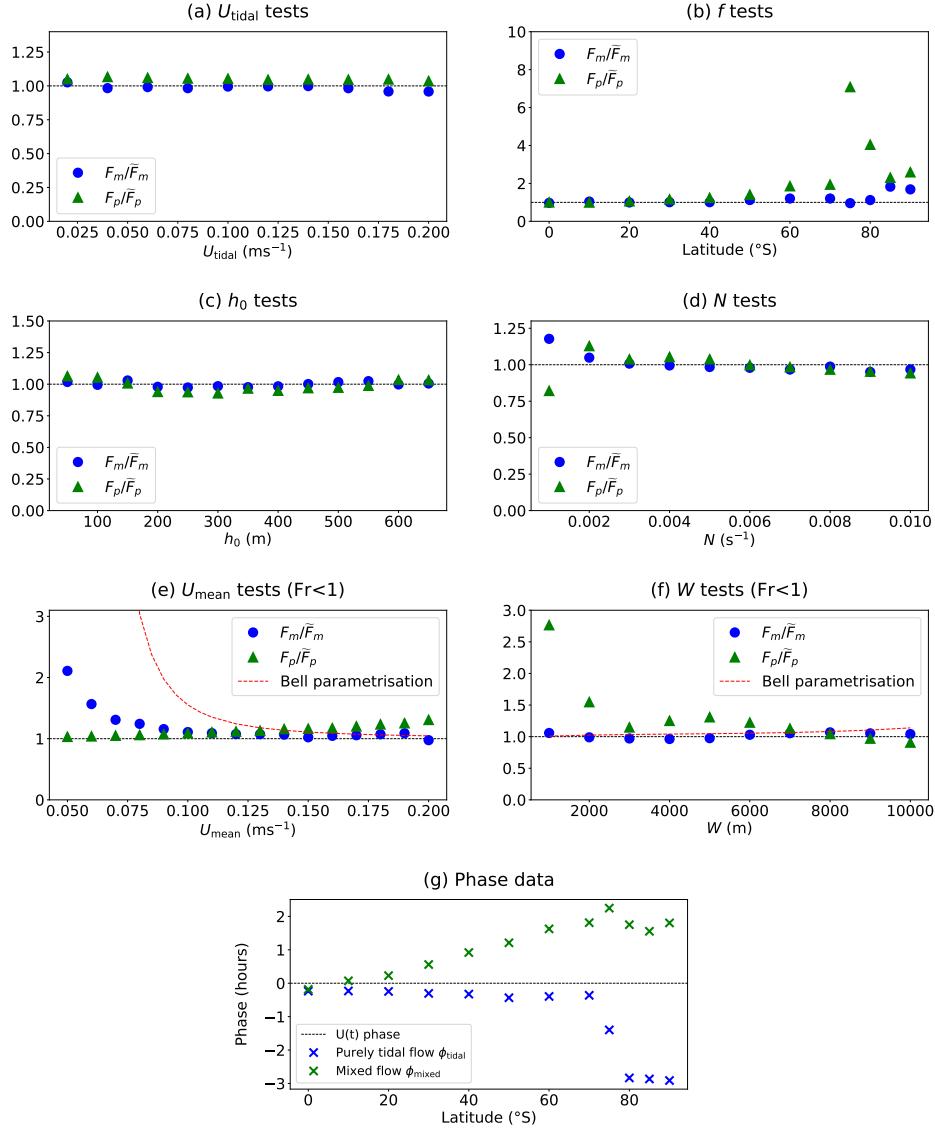
FIG. 8. Results for two-dimensional mixed flow simulations. In panels (a)–(d), the value of the ratios $F_m/\widetilde{F}_m$ and $F_p/\widetilde{F}_p$ are shown using $U_{\text{mean}} = 0.1$ ms^{-1} and the default parameters from our tidal tests (Figure 2). In panels (e) and (f), our results for low Froude numbers are displayed using $U_{\text{tidal}} = 0.1$ ms^{-1}, an M_2 tidal frequency, and the default parameters from our steady flow tests (Figure 5). In Figure (g), our results for the phase shift for both the tidal ($\widetilde{F}_P$) and mixed (F_P) cases are shown for the simulations that varied latitude (cf. Figure (b)). In each test, the uncertainty was always less than 10% (or less than 0.2 hours for Figure (g)) so the small error bars have been omitted.

5. Discussion and summary of suggested parametrisations

In the previous section, we tested existing topographic stress parametrisations for oceanic flows against a suite of simulations. Particular parametrisations of interest were those of Shakespeare et al. (2020) for tidal flows, as well as Bell (1975) and Klymak et al. (2010) for steady flows. Spanning a wide parameter space for an isolated Gaussian hill, we found that in many cases these parametrisations proved accurate, sometimes even when tested beyond their assumptions. In other cases, it was clear that an alternate parametrisation is required.

We also studied the case of a mixed flow in Sections 3e and 3f. Here, we primarily compared our simulation data against the naive parametrisation which assumes that the tidal and steady components of a flow are independent. Our data yielded the cases for which this naive parametrisation was accurate, and for which cases a more sophisticated parametrisation needs to be developed.

In what follows, we summarise our suggested parametrisations based on our results in Section 4. Here, as in
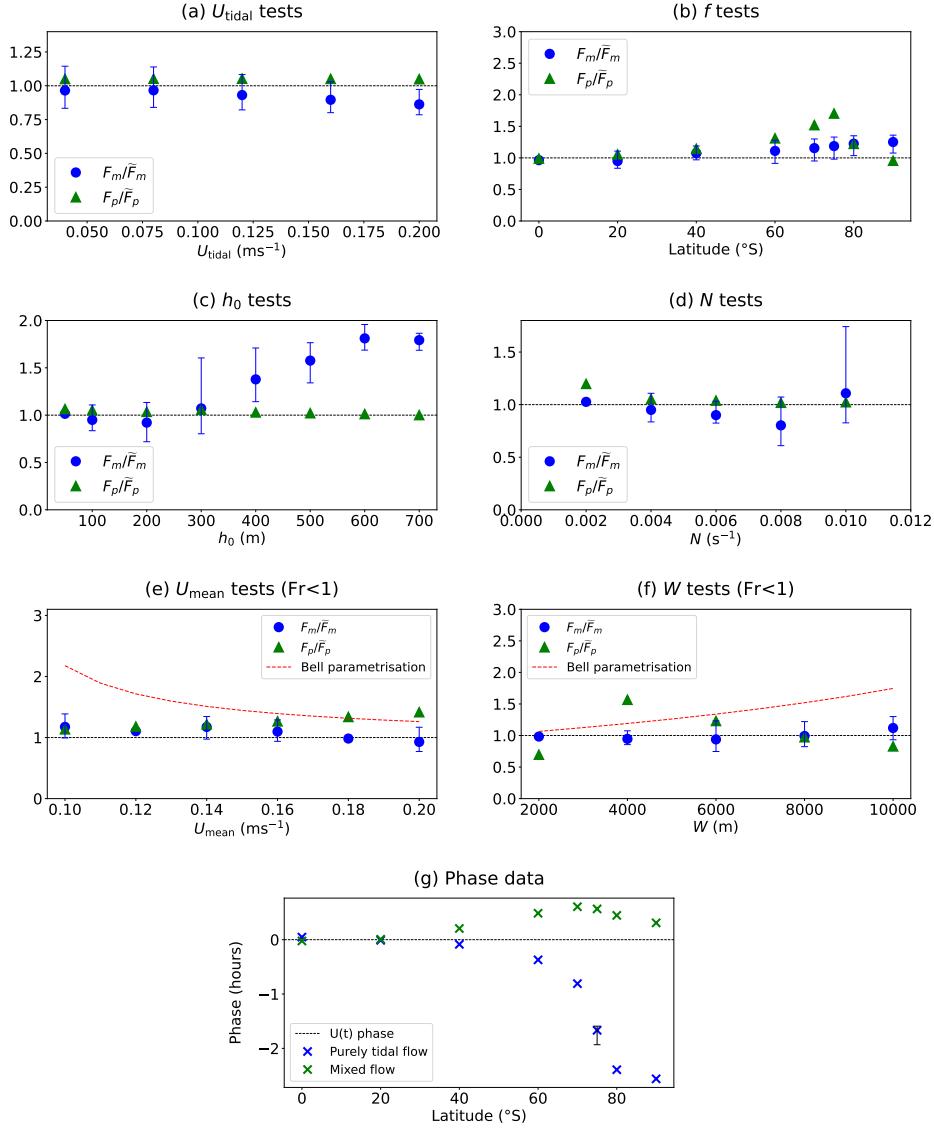
FIG. 9. Results for three-dimensional mixed flow simulations. In panels (a)–(d), the value of the ratios $F_m/\widetilde{F}_m$ and $F_p/\widetilde{F}_P$ are shown using $U_{\text{mean}} = 0.1 \text{ ms}^{-1}$ and the default parameters from our tidal tests (Figure 4). In panels (e) and (f), our results for low Froude numbers are displayed using $U_{\text{tidal}} = 0.1 \text{ ms}^{-1}$, an M_2 tidal frequency, and the default parameters from our steady flow tests (Figure 6). In Figure (g), our results for the phase shift for both the tidal ($\widetilde{F}_P$) and mixed (F_P) cases are shown for the simulations that varied latitude (cf. Figure (b)). In panels (a)–(f), error bars are only shown when the uncertainty is greater than 10%. In Figure (g), error bars are only displayed in the single case where the uncertainty was greater than 0.2 hours.

Section 2, F_{2d} and F_{3d} denote the stress in two and three dimensions respectively.

a. Suggested tidal flow parametrisations

For a purely tidal flow, we found that the parametrisations F_{SAH2d} (Equation (11)) and F_{SAH3d} (Equation (10) due to Shakespeare et al. (2020, 2021) were very accurate, mainly just requiring a small modification for large hill heights. In particular, for a purely oscillatory (tidal) flow

in two dimensions, we suggest setting

$$F_{2d} = \frac{H}{H - h_0} F_{\text{SAH2d}}, \qquad \text{if } h_0 \leq H/2,$$

$$F_{2d} = 2 F_{\text{SAH2d}}, \qquad \text{if } h_0 > H/2,$$

noting that this parametrisation may overestimate the stress

when $h_0 \approx H$.

In three dimensions, we then similarly suggest setting

$$F_{3d} = \frac{H}{H - h_0} F_{SAH3d}, \qquad \text{if } h_0 \leq H/2,$$

$$F_{3d} = 2 F_{SAH3d}, \qquad \text{if } h_0 > H/2,$$

for large hill widths W, where F_{SAH3d} is as in (10). From our testing, $W = 10000$ m was a sufficiently large width to notice this effect (with $h_0 = 100$ m). For more modest values of W, we instead suggest setting $F_{3d} = F_{SAH3d}$.

b. Suggested steady flow parametrisations

For a purely steady flow, we found that the parametrisations due to Bell (1975) and Klymak et al. (2010) had mostly accurate scalings, but required additional parameters to be accurate across a diverse set of regimes.

For a purely steady flow in two dimensions, we suggest setting

$$F_{2d} = \frac{1}{A_1 - B_1 \, Fr} F_{Bell2d}, \qquad \text{if } Fr \lesssim 1, \qquad (39)$$

$$F_{2d} = C_1 N h_0^2 U, \qquad \text{if } Fr \gg 1, \qquad (40)$$

where A_1, B_1 and C_1 are tunable constants, $Fr = N h_0 / U$, and F_{Bell2d} is as defined in (14). Our data gave the fitted values $A_1 = 0.71$, $B_1 = 0.46$ and $C_1 = 1.4$. Note that one can use the Taylor expansion of (39) for small Froude numbers ($Fr \ll 1$) to obtain an expression with polynomial dependence on Fr.

In three-dimensions, we then suggest setting

$$F_{3d} = \frac{1}{A_2 - B_2 |fW/U|} F_{Bell3d}, \quad \text{if } Fr \lesssim 1, \text{ and } |fW/U| \lesssim 1 \qquad (41)$$

$$F_{3d} = C_2 h_0 W U^2, \quad \text{if } Fr \gg 1, \qquad (42)$$

where similarly A_2, B_2 and C_2 are tunable constants, and F_{Bell3d} is as defined in (13). Our data gave the fitted values $A_2 = 1.34$, $B_2 = 0.88$ and $C_2 = 1$. Similar to (39), one could also change (41) to have a polynomial dependence on $|fW/U|$ if desired. Such an alternate form of (41) could be useful in the regime $A_2 - B_2 |fW/U| \approx 0$, in which (41) is unphysical.

c. Suggested mixed flow parametrisations

For a mixed flow

$$U(t) = U_{mean} + U_{tidal} \cos(\omega t) \qquad (43)$$

with associated stress (parallel to $U(t)$)

$$F_{2d} = F_m + F_p \cos(\omega t + \phi), \qquad \text{(two dimensions)}$$

$$F_{3d} = F_m + F_p \cos(\omega t + \phi), \qquad \text{(three dimensions)}$$

the naive parametrisation

$$F_m = \widetilde{F}_m, \qquad F_p = \widetilde{F}_p \qquad (44)$$

proved to be accurate for a wide range of parameters. Here, as in Sections 3e and 3f, $\widetilde{F}_m$ and $\widetilde{F}_p$ are the values of F_m and F_p if U_{tidal} or U_{mean} are set to be zero respectively. In two dimensions, the main regimes where (44) disagreed with our simulations were those near the critical latitude $|f| = \omega$, those with small values of U_{mean} (for F_m), and those with small values for W (for F_p). Then, in three dimensions, the naive parametrisation was again less accurate near the critical latitude $|f| = \omega$, and also for large hill heights h_0 (for F_m). Further work is required to accurately parametrise the stress in these specific cases.

In the bottom-trapped regime ($|f| > \omega$), the phase ϕ also notably disagreed with that predicted by the Shakespeare et al. (2020) theory for tidal flows, but still satisfied $\phi \approx 0$ for $|f| \ll \omega$.

6. Conclusion

We have evaluated existing stress parametrisations for tidal, steady and mixed flows over rough topography. In the case where the topography is an isolated Gaussian hill in two or three dimensions, we have directly compared these parametrisations with idealised numerical simulations. In some regimes, such as those with large scale topography, we find that existing parametrisations fall short. As a result, we have suggested new or improved parametrisations that more accurately match the simulation data. It is hoped that these new parametrisations may be used to more accurately model stress for mixed flows or other cases for which there is currently limited theory available. In future work, it would be insightful to perform a similar analysis in less-idealised settings with more complicated topography.

Data availability statement. Scripts that reproduce the simulations and all the data used in this paper are available at the repository github.com/DJmath1729/Ocean-hill-stress (Johnston 2025). Oceananigans is available at github.com/CliMA/Oceananigans.jl. pyestimate is available at github.com/alexishumblet/pyestimate.

References

Ansong, J. K., B. K. Arbic, M. C. Buijsman, J. G. Richman, J. F. Shriver, and A. J. Wallcraft, 2015: Indirect evidence for substantial damping

of low-mode internal tides in the open ocean. *Journal of Geophysical Research: Oceans*, **120 (9)**, 6057–6071.

Arbic, B. K., O. B. Fringer, J. M. Klymak, F. T. Mayer, D. S. Trossman, and P. Zhu, 2019: Connecting process models of topographic wave drag to global eddying general circulation models. *Oceanography*, **32 (4)**, 146–155.

Arbic, B. K., and Coauthors, 2018: Primer on global internal tide and internal gravity wave continuum modeling in HYCOM and MITgcm. *New Frontiers in Operational Oceanography*, 307–392.

Baker, L. E., and A. Mashayek, 2022: The impact of representations of realistic topography on parameterized oceanic lee wave energy flux. *Journal of Geophysical Research: Oceans*, **127 (10)**, e2022JC018 995.

Balmforth, N. J., G. R. Ierley, and W. R. Young, 2002: Tidal conversion by subcritical topography. *Journal of Physical Oceanography*, **32 (10)**, 2900–2914.

Bell, T. H., 1975: Topographically generated internal waves in the open ocean. *Journal of Geophysical Research*, **80 (3)**, 320–327.

Buijsman, M. C., B. K. Arbic, J. Green, R. W. Helber, J. G. Richman, J. F. Shriver, P. Timko, and A. Wallcraft, 2015: Optimizing internal wave drag in a forward barotropic model with semidiurnal tides. *Ocean Modelling*, **85**, 42–55.

Clark, M. R., and Coauthors, 2010: The ecology of seamounts: structure, function, and human impacts. *Annual Review of Marine Science*, **2**, 253–278.

Egbert, G. D., and R. D. Ray, 2000: Significant dissipation of tidal energy in the deep ocean inferred from satellite altimeter data. *Nature*, **405 (6788)**, 775–778.

Egbert, G. D., and R. D. Ray, 2001: Estimates of M2 tidal energy dissipation from topex/poseidon altimeter data. *Journal of Geophysical Research: Oceans*, **106 (C10)**, 22 475–22 502.

Falahat, S., and J. Nycander, 2015: On the generation of bottom-trapped internal tides. *Journal of Physical Oceanography*, **45 (2)**, 526–545.

Garner, S. T., 2005: A topographic drag closure built on an analytical base flux. *Journal of the Atmospheric Sciences*, **62 (7)**, 2302–2315.

Garrett, C., and E. Kunze, 2007: Internal tide generation in the deep ocean. *Annu. Rev. Fluid Mech.*, **39**, 57–87.

Harris, P. T., M. Macmillan-Lawler, J. Rupp, and E. K. Baker, 2014: Geomorphology of the oceans. *Marine Geology*, **352**, 4–24.

Humblet, A., 2024: pyestimate package, available at github.com/alexishumblet/pyestimate.

Jayne, S. R., and L. C. St. Laurent, 2001: Parameterizing tidal dissipation over rough topography. *Geophysical Research Letters*, **28 (5)**, 811–814.

Johnston, D. R., 2025: Base code for simulations, available at github.com/DJmath1729/Ocean-hill-stress.

Khatiwala, S., 2003: Generation of internal tides in an ocean of finite depth: analytical and numerical calculations. *Deep Sea Research Part I: Oceanographic Research Papers*, **50 (1)**, 3–21.

Kiss, A. E., and Coauthors, 2020: ACCESS-OM2 v1.0: a global ocean–sea ice model at three resolutions. *Geoscientific Model Development*, **13 (2)**, 401–442.

Klymak, J. M., 2018: Nonpropagating form drag and turbulence due to stratified flow over large-scale abyssal hill topography. *Journal of Physical Oceanography*, **48 (10)**, 2383–2395.

Klymak, J. M., D. Balwada, A. N. Garabato, and R. Abernathey, 2021: Parameterizing nonpropagating form drag over rough bathymetry. *Journal of Physical Oceanography*, **51 (5)**, 1489–1501.

Klymak, J. M., S. M. Legg, and R. Pinkel, 2010: High-mode stationary waves in stratified flow over large obstacles. *Journal of Fluid Mechanics*, **644**, 321–336.

Ledwell, J. R., E. T. Montgomery, K. L. Polzin, L. C. St. Laurent, R. W. Schmitt, and J. M. Toole, 2000: Evidence for enhanced mixing over rough topography in the abyssal ocean. *Nature*, **403 (6766)**, 179–182.

Llewellyn Smith, S. G., and W. R. Young, 2002: Conversion of the barotropic tide. *Journal of Physical Oceanography*, **32 (5)**, 1554–1566.

Lott, F., and M. J. Miller, 1997: A new subgrid-scale orographic drag parametrization: Its formulation and testing. *Quarterly Journal of the Royal Meteorological Society*, **123 (537)**, 101–127.

Melet, A., R. Hallberg, S. Legg, and M. Nikurashin, 2014: Sensitivity of the ocean state to lee wave–driven mixing. *Journal of Physical Oceanography*, **44 (3)**, 900–921.

Melet, A., R. Hallberg, S. Legg, and K. Polzin, 2013: Sensitivity of the ocean state to the vertical distribution of internal-tide-driven mixing. *Journal of Physical Oceanography*, **43 (3)**, 602–615.

Munk, W., and C. Wunsch, 1998: Abyssal recipes II: Energetics of tidal and wind mixing. *Deep Sea Research Part I: Oceanographic Research Papers*, **45 (12)**, 1977–2010.

Naveira Garabato, A. C., A. J. G. Nurser, R. B. Scott, and J. A. Goff, 2013: The impact of small-scale topography on the dynamical balance of the ocean. *Journal of Physical Oceanography*, **43 (3)**, 647–668.

Nikurashin, M., R. Ferrari, N. Grisouard, and K. Polzin, 2014: The impact of finite-amplitude bottom topography on internal wave generation in the Southern Ocean. *Journal of Physical Oceanography*, **44 (11)**, 2938–2950.

Peltier, W. R., and T. L. Clark, 1979: The evolution and stability of finite-amplitude mountain waves. Part II: Surface wave drag and severe downslope windstorms. *Journal of Atmospheric Sciences*, **36 (8)**, 1498–1529.

Perfect, B., N. Kumar, and J. J. Riley, 2020: Energetics of seamount wakes. Part II: Wave fluxes. *Journal of Physical Oceanography*, **50 (5)**, 1383–1398.

Ramadhan, A., and Coauthors, 2020: Oceananigans.jl: Fast and friendly geophysical fluid dynamics on GPUs. *Journal of Open Source Software*, **5 (53)**, 2018, doi:10.21105/joss.02018.

Sandstrom, H., and J. A. Elliott, 1984: Internal tide and solitons on the Scotian Shelf: A nutrient pump at work. *Journal of Geophysical Research: Oceans*, **89 (C4)**, 6415–6426.

Scinocca, J. F., and N. A. McFarlane, 2000: The parametrization of drag induced by stratified flow over anisotropic orography. *Quarterly Journal of the Royal Meteorological Society*, **126 (568)**, 2353–2393.

Shakespeare, C. J., 2020: Interdependence of internal tide and lee wave generation at abyssal hills: Global calculations. *Journal of Physical Oceanography*, **50 (3)**, 655–677.

Shakespeare, C. J., B. K. Arbic, and A. M. Hogg, 2020: The drag on the barotropic tide due to the generation of baroclinic motion. *Journal of Physical Oceanography*, **50 (12)**, 3467–3481.

Shakespeare, C. J., B. K. Arbic, and A. M. Hogg, 2021: The impact of abyssal hill roughness on the benthic tide. *Journal of Advances in Modeling Earth Systems*, **13 (5)**, e2020MS002 376.

Silvestri, S., and Coauthors, 2024: A GPU-based ocean dynamical core for routine mesoscale-resolving climate simulations. *ESS Open Archive*, doi:10.22541/essoar.171708158.82342448/v1.

Trossman, D. S., B. K. Arbic, S. T. Garner, J. A. Goff, S. R. Jayne, E. J. Metzger, and A. J. Wallcraft, 2013: Impact of parameterized lee wave drag on the energy budget of an eddying global ocean model. *Ocean Modelling*, **72**, 119–142.

Trossman, D. S., B. K. Arbic, J. G. Richman, S. T. Garner, S. R. Jayne, and A. J. Wallcraft, 2016: Impact of topographic internal lee wave drag on an eddying global ocean model. *Ocean Modelling*, **97**, 109–128.

Trossman., D. S., S. Waterman, K. L. Polzin, B. K. Arbic, S. T. Garner, A. C. Naveira-Garabato, and K. L. Sheen, 2015: Internal lee wave closures: Parameter sensitivity and comparison to observations. *Journal of Geophysical Research: Oceans*, **120 (12)**, 7997–8019.

Wagner, G. L., and Coauthors, 2025: High-level, high-resolution ocean modeling at all scales with Oceananigans. *arXiv preprint*, doi:10.48550/arXiv.2502.14148, 2502.14148.

Watts, A., 2019: Science, seamounts and society. *Geoscientist*, **290 (7)**, 10–16.

Winters, K. B., and L. Armi, 2014: Topographic control of stratified flows: Upstream jets, blocking and isolating layers. *Journal of Fluid Mechanics*, **753**, 80–103.